

PAPER • OPEN ACCESS

# Resonant interaction between runaway electrons and the toroidal magnetic field ripple in TCV

To cite this article: T.A. Wijkamp *et al* 2024 *Nucl. Fusion* **64** 016021

View the [article online](#) for updates and enhancements.

You may also like

- [Impact of microwave beam scattering by density fluctuations on the electron-cyclotron power deposition profile in tokamaks](#)  
J. Cazabonne, S. Coda, J. Decker et al.
- [Experimental validation of a Lyapunov-based controller for the plasma safety factor and plasma pressure in the TCV tokamak](#)  
B. Mavkov, E. Witrant, C. Prieur et al.
- [Overview of recent and current research on the TCV tokamak](#)  
S. Coda for the TCV Team

# Resonant interaction between runaway electrons and the toroidal magnetic field ripple in TCV

T.A. Wijkamp<sup>1,2,\*</sup> , M. Hoppe<sup>3,4</sup> , J. Decker<sup>4</sup> , B.P. Duval<sup>4</sup> , A. Perek<sup>4</sup> , U. Sheikh<sup>4</sup> , I.G.J. Classen<sup>2</sup> , R.J.E. Jaspers<sup>1</sup>  and the TCV team<sup>a</sup>

<sup>1</sup> Department of Applied Physics, Eindhoven University of Technology, Eindhoven 5600 MB, Netherlands

<sup>2</sup> DIFFER—Dutch Institute for Fundamental Energy Research, De Zaale 20, 5612 AJ Eindhoven, Netherlands

<sup>3</sup> School of Electrical Engineering and Computer Science, KTH Royal Institute of Technology, SE-11428 Stockholm, Sweden

<sup>4</sup> Ecole Polytechnique Fédérale de Lausanne (EPFL), Swiss Plasma Center (SPC), Lausanne, Switzerland

E-mail: [t.a.wijkamp@diffier.nl](mailto:t.a.wijkamp@diffier.nl)

Received 13 September 2023, revised 10 November 2023

Accepted for publication 17 November 2023

Published 24 November 2023



## Abstract

This work explains the anomalously high runaway electron (RE) pitch angles inferred in the flat-top of dedicated Tokamak à Configuration Variable (TCV) experiments. Kinetic modelling shows that the resonant interaction between the gyromotion of the electrons and the toroidal magnetic field ripple will give rise to strong pitch angle scattering in TCV. The resulting increase in synchrotron radiation power losses acts as a RE energy barrier. These observations are tested experimentally by a magnetic field ramp-down, which gradually reduces the resonant parallel momentum at which the REs interact with the ripple. Resulting changes in synchrotron emission geometry and intensity are observed using three multi-spectral camera imaging systems, viewing the RE beam at distinct spatial angles in multiple wavelength ranges. Experimental reconstructions of the RE distribution in momentum- and real-space are consistent with kinetic model predictions.

Keywords: runaway electrons, kinetic modelling, TCV, tokamaks, multi-spectral imaging

(Some figures may appear in colour only in the online journal)

## 1. Introduction

In magnetically confined nuclear fusion, superthermal electron formation can inhibit plasma startup [1] and threatens the

plasma-facing wall following plasma disruption events [2, 3]. Mitigation strategy design requires understanding the mechanisms governing momentum- and real-space dynamics of these so-called runaway electrons (REs). RE sensitive diagnostics on present-day tokamaks can be used to validate physics models of their velocity distribution and generation. Filtered camera imaging [4] of visible light synchrotron radiation observed in Tokamak à Configuration Variable (TCV) [5] was recently used to reconstruct the part of the RE distribution dominating the synchrotron emission in the visible-light [6, 7]. The inferred ratio between RE momenta perpendicular ( $p_{\perp}$ ) and parallel ( $p_{\parallel}$ ) to the magnetic field  $B$ , also described by the pitch angle  $\theta_p = \arctan(p_{\perp}/p_{\parallel})$ , was found inconsistent with

<sup>a</sup> See Reimerdes *et al* 2022 (<https://doi.org/10.1088/1741-4326/ac369b>) for the TCV Team.

\* Author to whom any correspondence should be addressed.



Original Content from this work may be used under the terms of the [Creative Commons Attribution 4.0 licence](https://creativecommons.org/licenses/by/4.0/). Any further distribution of this work must maintain attribution to the author(s) and the title of the work, journal citation and DOI.

a kinetic model describing RE electric field acceleration and plasma collisions [6]. Seemingly, other physical mechanisms are involved.

Herein, we demonstrate that the experimental synchrotron observations from TCV can be explained by pitch angle scattering of REs through a resonant interaction of their gyromotion with periodic variations in the toroidal magnetic field. We incorporate a diffusion operator [8] within a kinetic model [9] that predicts a strong conversion of  $p_{\parallel}$  to  $p_{\perp}$  for REs that reach a resonant parallel momentum  $p_{\parallel,n} \propto B/n$  [10], where  $n$  is the toroidal mode number. The scaling of the resonance location with the total magnetic field strength is used for experimental verification using a  $B$  ramp discharge. Distribution reconstructions from multi-camera, multi-wavelength imaging reveal that the momentum-space dynamics are consistent with our model.

## 2. Model for the RE distribution in the presence of a toroidal magnetic field ripple

The RE evolution in TCV is modelled using DREAM [9]. We prescribe a density  $n_e$  and temperature  $T_e$  of a fluid thermal electron bulk from experimental interferometry and Thomson scattering data and evolve a RE distribution  $f_{re}(\rho, p, \theta_p)$  and electric field on a discretised radial grid spanning normalised minor radii  $\rho$  up to the separatrix. The electric field is calculated self-consistently with the plasma current through a mean-field equation for the poloidal flux, using a loop voltage measurement at the tokamak wall as a boundary condition. The RE distribution is populated from the thermal bulk through effective Dreicer and avalanche generation rates [11, 12]. REs are added to the grid with  $p = 0$  since we do not kinetically resolve the Dreicer and avalanche generation. Collisions are modelled with an ultra-relativistic test-particle collision operator [13], in which we set  $v = c$ , since we are primarily interested in the REs with energies well beyond the critical runaway energy [9].

The kinetic equation solved for the REs takes the form [9]

$$\frac{\partial f_{re}}{\partial t} = \sum_{x,y} \frac{1}{\mathcal{V}'} \frac{\partial}{\partial z^x} \left[ \mathcal{V}' \left( -\{A^x\} f_{re} + \{D^{xy}\} \frac{\partial f_{re}}{\partial z^y} \right) \right] + \{S\}, \quad (1)$$

where the advection components  $A^x = (\partial z^x / \partial \mathbf{z}) \cdot \mathbf{A}$  include electric field acceleration, collisional friction, bremsstrahlung reaction forces and synchrotron radiation. The diffusion term (in dyadic notation)  $D^{xy} = (\partial z^x / \partial \mathbf{z})(\partial z^y / \partial \mathbf{z}) : \mathbf{D}$  accounts for the collisional momentum-space diffusion, and pitch angle diffusion through the ripple interaction as described below. The source term  $S$  is used to add new REs to the grid from the fluid generation rates. Curly brackets denote bounce averaging over toroidal angle  $\varphi$ , gyrophase and poloidal angle  $\theta$ . Finite Larmor radius and cross-field drift effects are ignored. Summation is over the constants of motion  $\mathbf{z} = (r, p, \xi)$  being the minor radius which serves as a flux-surface label, momentum and pitch, where  $\xi = \cos(\theta_p)$ .  $\xi$  is evaluated at the point of minimum magnetic field on a given flux-surface,

the radial coordinate at  $\theta = 0$ , and  $\mathcal{V}'$  denotes the phase-space Jacobian.

In this work, a diffusion operator is added for pitch angle scattering of REs due to a resonant interaction of their gyromotion with periodic variations in the toroidal magnetic field strength. Misalignment of the gyro-orbit averaged RE momentum vector with the perturbed magnetic field results in a Lorentz force, which induces a reversible periodic exchange between  $p_{\parallel}$  and  $p_{\perp}$ . However, if the RE gyrofrequency  $\omega_{ce}$  approaches the frequency with which the electron experiences a ripple, a second-order correction term to the time derivative of  $p_{\perp}$  becomes important. This gives rise to a strong increase in pitch angle for REs satisfying  $p \approx p_{\parallel,nm}$  and  $p < p_{\parallel,nm}$  [8]. The resonant momenta  $p_{\parallel,nm}$  are obtained by equating the RE gyrofrequency with the effective wave number of the ripple  $k_{nm}$ . The latter has a toroidal component determined by the distance between the coils, expressed as a function of the toroidal circumference  $L_{\varphi} = 2\pi R$ , where  $R$  is the major radial coordinate, and the number of coils  $N_c$ . The poloidal component is related to the poloidal circumference of the flux-surface  $L_{\theta}$ . Therefore one gets

$$\frac{eB}{p_{\parallel}} = \mathbf{k}_{nm} \cdot \frac{\mathbf{B}}{B} \quad (2)$$

$$\mathbf{k}_{nm} = 2\pi \left( \frac{N_c n}{L_{\varphi}} \hat{\varphi} + \frac{m}{L_{\theta}} \hat{\theta} \right),$$

with electron charge  $e$ . Writing the magnetic field in the symplectic form [14]

$$\mathbf{B} = G(r) \nabla \varphi + \frac{1}{2\pi} \nabla \varphi \times \nabla \psi(r), \quad (3)$$

with magnetic poloidal flux  $\psi$  and  $G$  describing the toroidal field, we obtain

$$\mathbf{k}_{nm} \cdot \frac{\mathbf{B}}{B} = \frac{1}{B} \left( \frac{N_c n G}{R^2} + \frac{m}{L_{\theta}} \frac{\nabla \theta}{|\nabla \theta|} \cdot (\nabla \varphi \times \nabla \psi) \right). \quad (4)$$

Neglecting the poloidal field term, which amounts to a small correction, using  $B = G/R$ , we obtain in the small pitch angle limit, where  $p_{\parallel}$  varies little along the particle trajectory, the following resonance condition:

$$p_{\parallel,nm} = \frac{eG(r)}{N_c n} = \frac{eBR}{N_c n}. \quad (5)$$

Equation (5) highlights the dependence of the resonant momentum on the magnetic field magnitude.

Accounting for a reduction in pitch angle scattering efficiency due to an incoherent walk in RE gyration phase as a result of RE-plasma collisions, the process can be described as diffusion in momentum-space. In dyadic notation, where  $\mathbf{D}, \mathbf{I}$  are matrices, it was derived in earlier work that [8]

$$\mathbf{D} = (\mathbf{I} - \mathbf{p}\mathbf{p}/p^2) D_{\perp, \text{ripple}} \quad (6)$$

$$D_{\perp, \text{ripple}} = \frac{\pi}{32} \frac{eBv_{\parallel}}{m_e c} \left( \frac{\delta B_{nm}}{B} \right)^2 H_{nm},$$

with rest mass  $m_e$ , speed of light  $c$ , magnetic field ripple mode amplitudes  $\delta B_{nm}/B$ , a resonance width function  $H_{nm}(p_{\parallel})$  and parallel RE velocity  $v_{\parallel}$ . The pitch angle diffusion term, added to the kinetic equation (1), is given by:

$$D^{\xi_0 \xi_0} = |\nabla \xi_0|^2 D_{\perp, \text{ripple}} = \frac{B_{\min}}{B} \frac{\xi^2}{\xi_0^2} \frac{1 - \xi_0^2}{p^2} D_{\perp, \text{ripple}} \quad (7)$$

For the width function  $H_{nm}$  we assume a Gaussian shape

$$H_{nm} = \frac{2}{\sqrt{\pi} \Delta p_{\parallel, nm}} \exp \left( -\frac{(p\xi - p_{\parallel, nm})^2}{(\Delta p_{\parallel, nm})^2} \right) \quad (8)$$

$$\Delta p_{\parallel, nm} = p_{\parallel, nm} \sqrt{\frac{\delta B_{nm}}{B} \sqrt{1 - \xi^2}}$$

To approximate the ripple strength, an infinite straight line conductor model for a tokamak with toroidal field coils at minor radius  $r_c$  is used [15, 16]. Considering only the first poloidal harmonic:

$$\frac{\delta B_{n1}}{B} = \frac{1}{2} \exp \left( -\frac{N_c n (r_c - r)}{r_c + R_0} \right), \quad (9)$$

with  $R_0$  the plasma axis major radius. The ripple strength decreases exponentially with increasing mode number. Also, REs in orbits at larger minor radius, closer to the toroidal field coils, experience a stronger ripple and associated scattering.

To illustrate the effect of ripple scattering on the RE momentum-space distribution, DREAM is run with experimental input from TCV experiment #76462. The diverted plasma scenario has a plasma electron temperature, electron density and applied loop voltage typical of non-disruptive TCV RE experiments [17]. A detailed description is deferred to the next section. In figure 1 the time evolution of the RE momentum-space distribution at a normalised minor radius  $\rho$  of 0.45 is shown. Initially, the distribution extends towards increasingly high momenta due to electric field acceleration, evident from comparing figures 1(a) and (b). Since the acceleration is primarily parallel to the magnetic field, the distribution becomes increasingly peaked at low pitch angles with increasing momentum.

In figure 1(c), the most energetic REs have reached parallel momenta where they interact with the primary ripple mode ( $n = 1$ ). These electrons undergo a quick diffusion in pitch angle space. Power loss due to synchrotron radiation increases with the conversion of parallel to perpendicular momentum, effectively acting as an energy-limiting mechanism. In momentum-space, the scattered REs are trapped in a strongly radiating momentum-space vortex.

In support of a detailed description of the momentum-space dynamics, figure 2 shows a close-up of the vortex in  $p_{\perp}, p_{\parallel}$ -space. REs at low  $p_{\perp}$  enter the ripple interaction region, indicated by the dashed black contour line, close to the resonant parallel momentum  $p_{\parallel, nm}$ . If the pitch angle diffusion is much stronger than the electric field momentum advection, the electrons start moving along a momentum-space trajectory of approximately constant total momentum. Parallel momentum is exchanged for perpendicular momentum until  $p_{\parallel}$  is sufficiently removed from  $p_{\parallel, nm}$  to have the RE escape the ripple

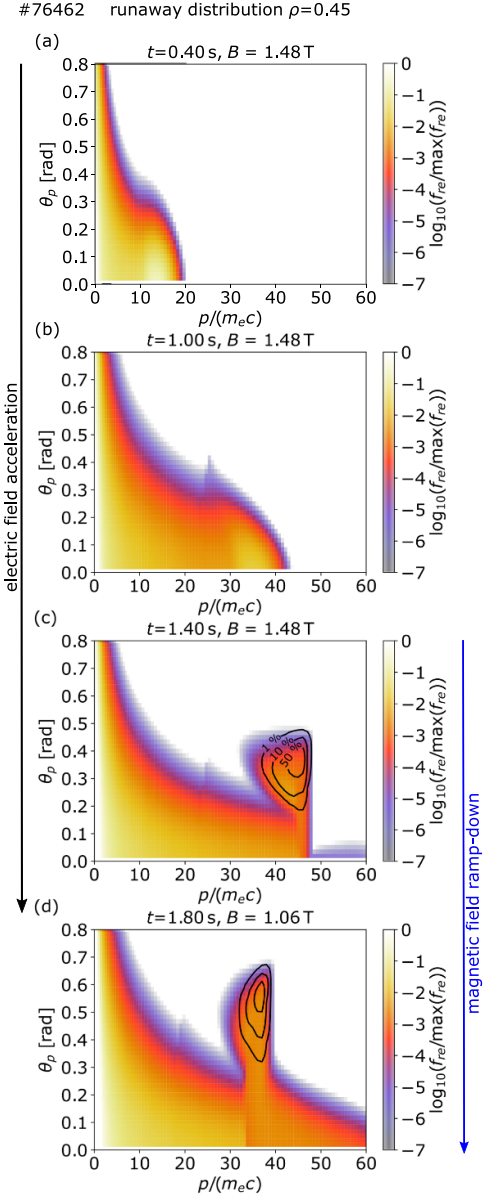


**Figure 1.** DREAM RE momentum-space distribution ( $\rho = 0.45$ ) evolution for TCV RE experiment #76462. Electric field acceleration initially drives the distribution to higher momenta (a), (b). When the ripple-resonant parallel momentum is reached, pitch-angle scattering sets in (c). After  $t = 1.4$  s, the magnetic field strength is ramped down, lowering the resonant momentum (c), (d). The black contour lines (c), (d) indicate fractions of the peak visible light radiance in momentum-space.

interaction region. In this part of momentum-space, RE synchrotron radiation losses overcome electric field momentum gain so that the total momentum starts decreasing. When the particles cross the boundary where electric field acceleration becomes dominant (solid black line), they are re-accelerated to the ripple resonance, where the process is repeated. The momentum-space structure described here shows similarities to those predicted to arise from collisional pitch angle scattering at much larger momenta in TCV [18–20] or due to the interaction of REs with whistler waves [21].

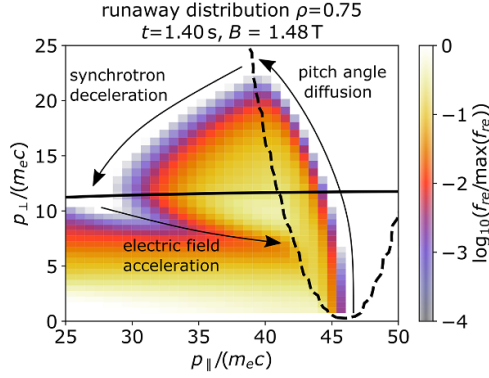


**Figure 2.** Close examination of a RE vortex from a kinetic simulation for TCV experiment #76 462 ( $\rho = 0.75$ ). The solid black line indicates the boundary in momentum-space below which electric field acceleration dominates and above which synchrotron radiation power losses take over. The dashed black contour line indicates a constant level of the ripple diffusion strength.

Ripple location dependence on the magnetic field strength, see equation (5), is portrayed in figure 1 where the DREAM simulation RE vortex at magnetic fields of (c) 1.48 T and (d) 1.06 T is shown. The black contour lines indicate what part of the vortex radiates most strongly in the visible wavelengths. The percentages, indicated in figure 1(c), are with respect to the peak contribution value in momentum-space. With decreasing field strength, the ripple-resonant momentum decreases in proportion according to equation (5), shifting the vortex to significantly lower momenta. Simultaneously, the balance between the shifting ripple resonance region and a decreasing synchrotron power at lower  $B$  allows for higher RE vortex pitch angles.

The vortex location has a radial dependence through the sensitivity of  $p_{\parallel, nm}$  to the mean  $B$ -field along the RE orbit. For the case at hand, the core value of  $p_{\parallel, 11}/m_e c$  exceeds that in the edge by around 4% as a result of a decrease in the average magnetic field moving from core to edge. Furthermore,  $\delta B/B$  is larger at the edge following equation (9). This means that edge REs will experience a strong ripple at  $p_{\parallel}$  further removed from the resonance and convert more of their momentum to  $p_{\perp}$ . As a result, the vortex as a whole moves to lower momenta and higher pitch angles, amplifying the radial dependence.

### 3. Experimental scan of the ripple-resonant RE momentum in TCV

In this section, we describe the TCV experiment #76 462 in more detail. It was devised to test the hypothesis that toroidal field ripple scattering is the underlying phenomenon behind the anomalously high inferred RE pitch angles [6, 7]. Since pitch angle scattered REs are strongly radiating in the visible part of the spectrum, camera imaging is well suited for probing this part of the RE distribution. Both the directionality of the emission and its optical spectrum depend on the distribution of REs in space and momentum [22]. As a result, we can reconstruct the distribution from synchrotron emission

through forward [23] and backward [7] methods, using a synthetic diagnostic model [24].

This work uses three optical cavity-based multi-spectral MANTIS imaging systems [4], installed at three different heights in the same toroidal sector of TCV. The three systems have a toroidal view of the plasma in the direction opposing that of the RE movement, allowing detection of the highly directional synchrotron radiation. The MANTIS systems each have 6–10 cameras, of which 8 in total are equipped with dedicated synchrotron filters [7]. Thus, the setup provides extensive spatial resolution at multiple spectral ranges, maximally constraining the distribution reconstruction problem [7].

As shown in the previous section, see figures 1(c) and (d), both the momentum and pitch angle at which the RE vortex is centred are sensitive to the magnetic field magnitude. Thus, ramping down the toroidal magnetic field after forming a RE beam should result in detectable changes in recorded synchrotron images. Figure 3 gives an overview of TCV experiment #76 462, run in diverted plasma geometry. Herein, a low electron density  $n_e$  phase lasting until time  $t = 0.4$  s, see figure 3(b), ensures a high ratio of the electric field to Dreicer field as depicted in figure 3(d), so that part of the electron population enters the RE regime through Dreicer generation. The PMTX photomultiplier x-ray detector signal in figure 3(c) indicates the presence of REs throughout the remainder of the flat-top phase. Subsequently, we increase  $n_e$  to allow for higher loop voltage (figure 3(d)) at constant plasma current, see figure 3(e), accelerating the existing RE population towards the ripple-resonant momentum. At  $t = 1.4$  s we start ramping down the toroidal magnetic field in figure 3(f) from  $t = 1.48$  T on the magnetic axis to 1.06 T to shift the RE vortex in momentum-space. Simultaneously, the plasma current is ramped down at the same relative rate, from 180 kA to 130 kA, to conserve the magnetic geometry and avoid RE-expelling instabilities.

The time evolution of the, filter transmission band normalised, recorded synchrotron radiance  $\Phi$  is shown in figure 4. The first faint traces of a visible-light synchrotron pattern can be distinguished on the camera with the highest signal-to-noise ratio at  $t = 0.96$  s. We compare this against a simple maximum momentum  $p_{\max}$  estimate obtained by integrating the experimental loop voltage over time, starting at the time of lowest  $n_e$  ( $t = 0.31$  s) when we expect most REs to be formed. Close agreement is found, with  $p_{\max}$  reaching the  $n = 1$  plasma edge resonant momentum of  $p_{11}/m_e c = 46$  at  $t = 1.00$  s.

Between the emission onset and the start of the  $B$ -ramp at  $t = 1.4$  s, the radiance first increases on all cameras and then settles towards an equilibrium. Comparing the filter radiance traces for filters at different wavelengths in figure 4 we find that the synchrotron intensity decreases with decreasing wavelength. This agrees with synchrotron radiation peaking in the infrared, as expected for this magnetic field strength and RE energies. Note that while intensity increases, there is little change in the shape of the synchrotron pattern on the camera sensor.

During the  $B$  ramp-down, the synchrotron patterns start moving and deforming as expected. In figure 5 lower-port (a) mid-port (b) and top-port (c) synchrotron images at the start of



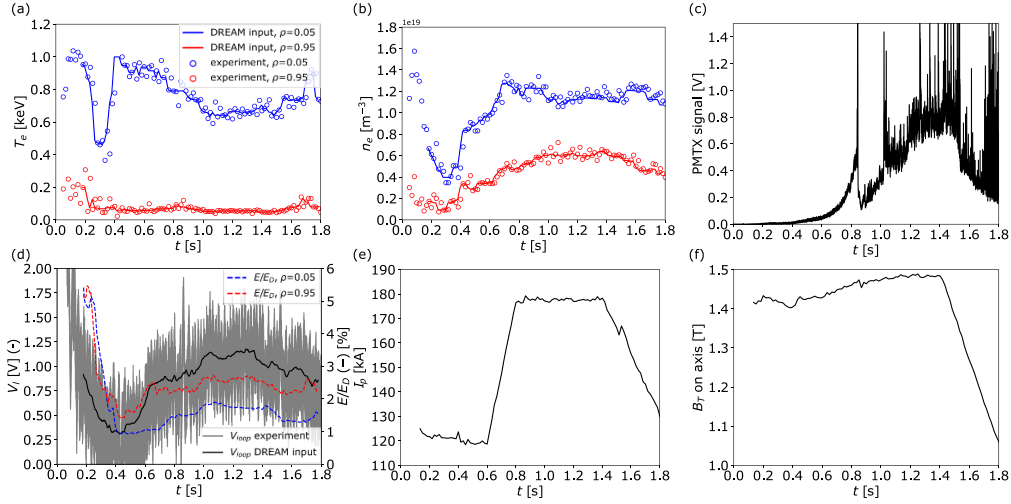


**Figure 3.** Experimental data from TCV quiescent RE experiment #76462. (a) Electron temperature in the core and edge as measured using Thomson scattering. The smoothed curve shows the corresponding input into DREAM. (b) Electron density measurement from Thomson scattering corrected by far infrared interferometry. (c) PMTX photomultiplier tube signal showing x-rays from the RE population. (d) Loop voltage recorded, with smoothed input into DREAM. The plot also shows the ratio of the electric field to Dreicer field computed by DREAM. (e) Total plasma current. (f) Toroidal field magnitude on the magnetic axis.

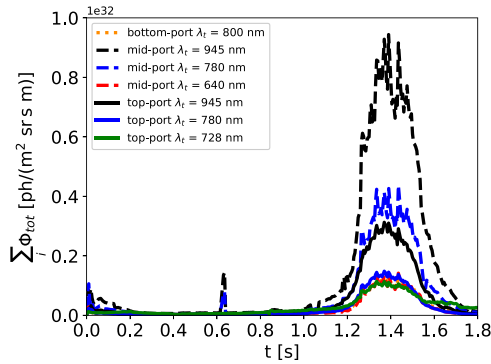


**Figure 4.** Total radiance (summed over all pixels) divided by the wavelength integrated filter transmission curves for all MANTIS cameras in discharge #76462. Camera position and the filter central transmission wavelengths  $\lambda_t$  are indicated.

the ramp (top row) are compared against those halfway into the scan (bottom row). For the lower- and top-port systems, a clear shift in radiance distributions across the pattern is observed. On the mid-port the main change is a shift towards the high-field-side, indicative of an increasing pitch angle.

#### 4. Verification of the magnetic field ripple scattering hypothesis

For quantitative statements on the RE distribution behind the synchrotron patterns reported in section 3, we rely on the synthetic diagnostic SOFT. We refer to earlier work for the procedure of constructing such a model and the underlying

assumptions [24], and iterate that SOFT can provide a Green's function matrix  $\mathbf{GJ}$ , which links a column matrix representation of the RE distribution function  $\mathbf{f}(\rho, \mathbf{p}, \theta_p)$ , the phase-space parameters are likewise 1D column matrices, to a pixel-dependent radiance column matrix  $\Phi$  on the camera

$$\Phi = \mathbf{GJ} \cdot \mathbf{f}, \quad (10)$$

where the row-dimension of  $\mathbf{GJ}$  corresponds to the pixels, and the column-direction to the RE phase-space. The spectral and spatial resolution provided by the MANTIS systems facilitates a direct reconstruction of  $\mathbf{f}$  from a set of filtered camera images. Information from multiple cameras is combined by aggregating the radiances and Green's functions into a single system of equations. Here we present a reconstruction algorithm with improved performance as compared to that detailed in earlier work [7]:

- (1) First, an initial estimate of the distribution function is made in the form:

$$\begin{aligned} \mathbf{f} &= \mathbf{f}_\rho(\rho) \cdot \mathbf{f}_{p/\theta_p}(\mathbf{p}, \theta_p) \\ &= \mathbf{f}_\rho \cdot \exp\left(\frac{-(\mathbf{p} - \tilde{\mathbf{p}})^2}{2\tilde{\sigma}_p^2}\right) \cdot \exp\left(\frac{-(\theta_p - \tilde{\theta}_p)^2}{2\tilde{\sigma}_{\theta_p}^2}\right). \end{aligned} \quad (11)$$

It is assumed that the momentum-space distribution  $\mathbf{f}_{p/\theta_p}$  has the same shape for all minor radii, but the total number of REs has a radial dependence  $\mathbf{f}_\rho$ . The Gaussian shape of  $\mathbf{f}_{p/\theta_p}$  is a rough approximation for a RE vortex. An iterative two-step fit is performed:

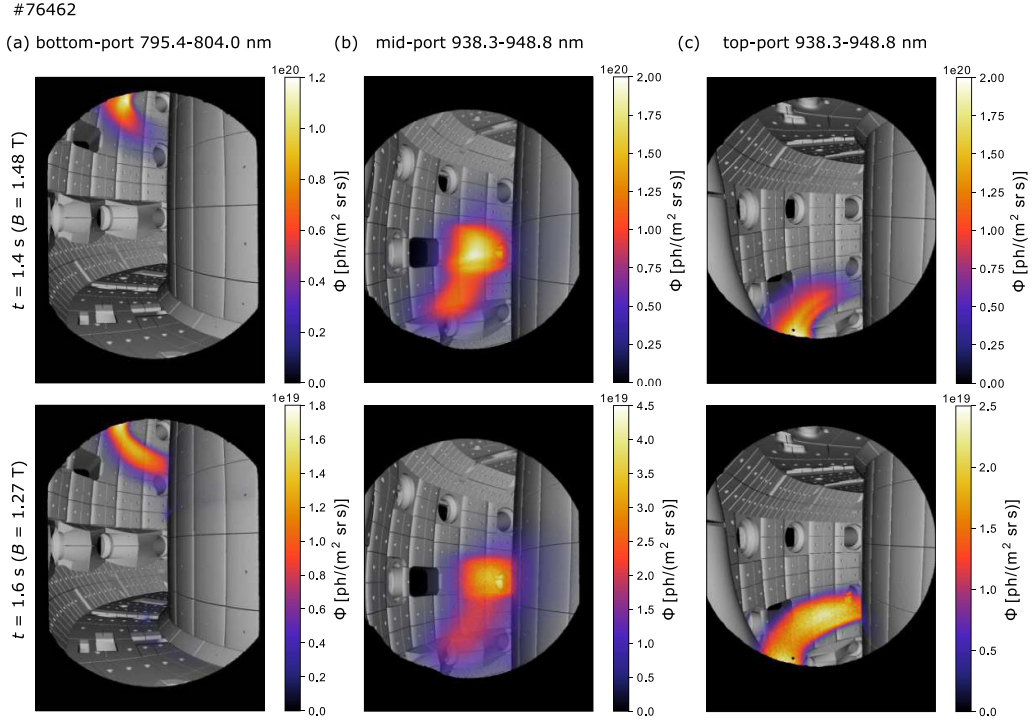


**Figure 5.** Synchrotron images, overlaid on the TCV CAD model, from the bottom-port (795.4–804.0 nm) (a), mid-port (938.3–948.8 nm) (b) and top-port (938.3–948.8 nm) (c) MANTIS systems for discharge #76462. The frames at  $t = 1.4$  s (top-row) were recorded at an on-axis  $B$ -field of 1.48 T, and those at  $t = 1.6$  s (bottom-row) at 1.27 T.

- (i) A best-fit combination of central momentum  $\tilde{p}$ , central pitch angle  $\tilde{\theta}_p$  and momentum and pitch angle vortex widths  $\tilde{\sigma}_p$  and  $\tilde{\sigma}_{\theta_p}$  is found by scanning over a range of plausible values. For every combination, the normalised synthetic images from SOFT are compared against the experimental data [23]. A fixed  $\mathbf{f}_\rho$ , initially assumed uniform, is used.
- (ii) Fixing  $\mathbf{f}_{p/\theta_p}$  to the best-fit shape,  $\mathbf{f}_\rho$  is updated using the SART algorithm [25], converging to a best absolute match between the experimental and synthetic images. This procedure is repeated until a pre-set convergence level of the distribution is reached.
- (2) Starting from the approximate solution obtained in the previous step, an adaptive version [26, 27] of L2-regularised SART [28] is used to iteratively descend to a solution for  $\mathbf{f}$ . This allows for radial dependence of the momentum-space distribution:

$$\mathbf{f}^{k+1} = \mathbf{f}^k + \lambda_r [(\mathbf{G}\mathbf{J}^T \odot \mathbf{f}^k) \cdot ((\Phi - \mathbf{G}\mathbf{J} \cdot \mathbf{f}^k) \odot (\mathbf{G}\mathbf{J} \cdot \mathbf{f}^k + \alpha_r))] \odot (\mathbf{G}\mathbf{J}^T \cdot \mathbf{I}), \quad (12)$$

where  $\lambda_r$  is a relaxation parameter (typically 1),  $\alpha_r$  a regularisation parameter here set to the maximum synthetic pixel value at each iteration,  $\mathbf{I}$  is a column matrix identically equal to 1,  $\odot$  denotes column-wise multiplication and  $\oslash$  is element-wise division.

Synthetic reconstructions of the experimental synchrotron images in figure 5 are shown in figure 6. The temporal evolution of the radiance intensity distributions on all cameras and filter ranges are replicated. The only apparent mismatch is in the lower lobe of the pattern on the mid-port channel (b). Inspection of the reconstructed distribution and camera Green's functions indicates that the sharp granular feature in the synthetic image originates from an isolated low pitch angle contribution. This contribution is likely a reconstruction artefact arising from a spatial calibration or magnetic equilibrium inaccuracy, which makes it complicated for the reconstruction algorithm to explain some radiation features at the very edge of the synchrotron pattern. The sum of the absolute error in the pixel values normalised to the sum of the experimental images is  $0.3 \pm 0.1$  throughout the start of the magnetic field ramp. Sources of error are discussed in section 5.

The reconstruction is applied to synchrotron images throughout the magnetic field ramp-down in experiment #76462 from 1.48 T to 1.15 T. Below this range, some of the synchrotron patterns are not bright enough for the reconstruction algorithm. The reconstructed momentum-space distribution for  $t = 1.60$  s is shown in figure 7, where the black and orange contour lines bound the region of momentum-space contributing to visible synchrotron emission at 1% or more of the peak value for the experimental reconstruction and DREAM model respectively (similar to the contour lines in figures 1(c) and (d)). Outside this region, the distribution does not contribute sufficiently to the recorded camera images to be reconstructed. The experiment and model

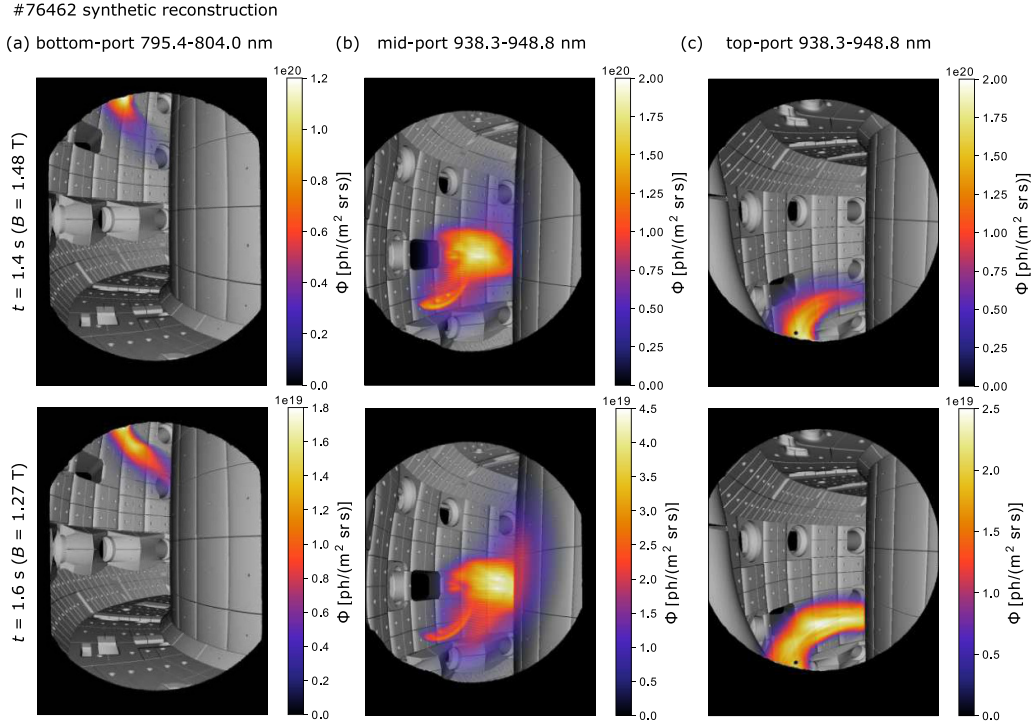


**Figure 6.** Synthetic synchrotron images, overlaid on the TCV CAD model, from the bottom-port (795.4–804.0 nm) (a), mid-port (938.3–948.8 nm) (b) and top-port (938.3–948.8 nm) (c) MANTIS-type systems for discharge #76 462 at  $t = 1.4$  s ( $B = 1.48$  T).

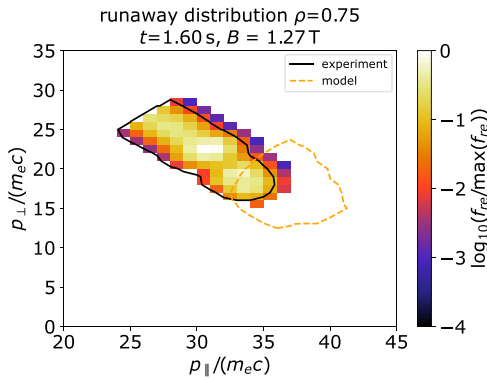


**Figure 7.** Normalised reconstructed RE distribution ( $\rho = 0.75$ ) for  $t = 1.60$  s in experiment #76 462. The black contour line bounds the region of momentum-space where the emission in the visible exceeds 1% of the peak emission, whereas the orange contour line does the same for the DREAM distribution.

show good agreement in terms of the total momentum, but the experimental reconstruction hints at a more efficient conversion of  $p_{\parallel}$  to  $p_{\perp}$ . Furthermore, the reconstructed part of the distribution stretches out along a trajectory of constant  $p$ , consistent with strong pitch angle diffusion.

Reconstruction results for the whole  $B$  ramp-down are compared to numerical predictions in figure 8. Figure 8(a) depicts the average momentum  $p_c$  of REs contributing to the visible light radiation at  $\rho^* = 0.75$ , which is defined here as:

$$p_c = \int (GJf_e)_{p,\rho=\rho^*} p dp / \int (GJf_e)_{p,\rho=\rho^*} dp, \quad (13)$$

where  $(GJf_e)_{p,\rho=\rho^*}$  is the product of the Green function and reconstructed RE distribution at  $\rho = \rho^*$  integrated over pitch angle. Both kinetic model results (crosses, orange) and experimental inferences (dots, blue) are shown. The bars indicate the width of the momentum-space region contributing more than 50% of the peak emission. The same is shown for the average contributing pitch angle  $\theta_{p,c}$  in figure 8(b):

$$\theta_{p,c} = \int (GJf_e)_{\theta_p,\rho=\rho^*} \theta_p d\theta_p / \int (GJf_e)_{\theta_p,\rho=\rho^*} d\theta_p. \quad (14)$$

The reconstructed momentum of peak emission for the RE vortex shows close agreement to the ripple model. A  $p/(m_e c)$  shift from 42 to 37 between 1.48 T and 1.16 T is found, deviating from modelling results by only  $p/(m_e c) = 1.2 \pm 0.6$  (standard deviation) if all acquired synchrotron images are considered. The high pitch angle values and dependence on  $B$  are also qualitatively replicated, although the reconstructed values exceed the modelled ones by  $0.14 \pm 0.02$  rad. In the next section, we discuss the degree to which these results support the ripple pitch angle scattering model.

While the reconstruction algorithm described herein returns a radial distribution, no quantitative comparison is made to our kinetic model, which does not include radial transport. All that is reported here is that in the experiment  $\mathbf{f}$  is found to decrease with minor radius. This is in qualitative agreement with the



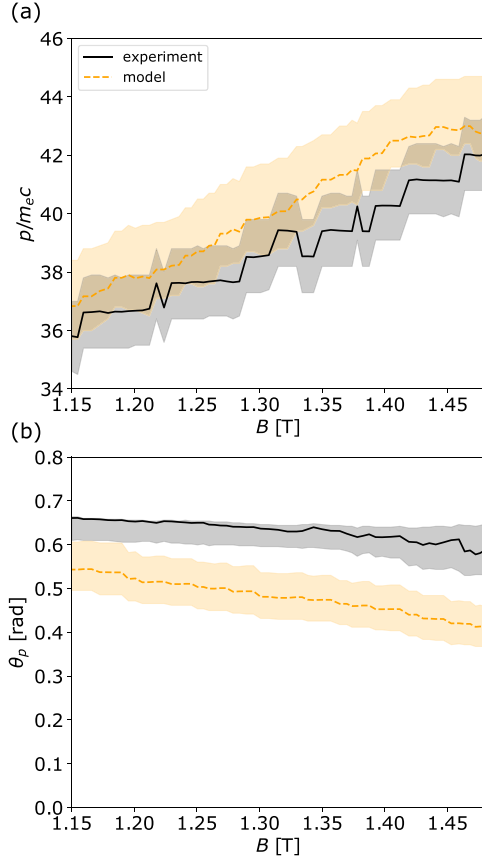


**Figure 8.** Magnetic field dependence of the momentum-space point at which the  $\rho = 0.75$  RE vortex in experiment #76462 radiates most strongly in the visible spectrum. (a) The dashed orange line indicates the peak momentum predicted by kinetic modelling, and the solid black line the experimentally inferred values. The shaded regions indicate the vortex width, defined as the region radiating at more than 50% of the peak value. (b) The same is depicted for the vortex pitch angle.

DREAM modelling predicting that RE generation is largest near the plasma core.

## 5. Discussion

We assess the degree of consistency between the experimentally inferred RE distribution and that predicted by kinetic modelling. Firstly, the main model uncertainties are discussed, being the ripple strength (equation (9)) and width (equation (8)).

In this work, we employ an orbit-averaged simplistic infinite straight-line conductor model for the ripple magnitude. For more accurate estimates of the vortex pitch angle, detailed RE orbit tracking [29] could be used in the future to refine the ripple description and capture its RE momentum dependence through the drift orbit shift. For the present work, the sensitivity of the model output to  $\delta B/B$  was assessed. Increasing the ripple strength raises vortex pitch angles, and decreases the momentum, in accordance with the discrepancy found between experimental results and modelling. However,

unrealistic values of  $\delta B/B$  are required to bridge the gap in vortex pitch angle and result in modelled vortex momenta well below the experimental values.

The ripple width model is a more plausible candidate for model mismatch. There is no guarantee that the Gaussian envelope adopted is the most accurate functional form for the width operator. While the parallel momentum at which REs enter the vortex is only weakly affected by an increase in  $\Delta p_{\parallel, nm}$ , conversion of  $p_{\parallel}$  to  $p_{\perp}$  is sensitive to this parameter. Doubling the resonance width, the momentum value at peak emission decreases only a little, while the pitch angle increases by 0.1 rad, bringing it to agreement with the experiment.

Another explanation for the pitch angle discrepancy is the absence of RE-invoked plasma instabilities in the model. Strong RE distribution momentum-space gradients are believed to drive instabilities leading to pitch-angle scattering [30], which could explain the underestimated vortex pitch angle.

The origins of deviations between experimental and synthetic images were detailed in earlier work [7]. Limitations to the SART algorithm used were found to be dominant followed by uncertainties in the spatial calibration of the cameras.

Alternative explanations for the observed change in synchrotron emission shape during the  $B$ -ramp, which affect the interpretation presented here, have been explored. Toroidal field changes affect the magnetic field geometry and, therefore, the synchrotron directionality. However, since  $I_p$  was ramped down at the same rate as  $B$ , the geometric effects are expected to be negligible. Furthermore, when reducing  $B$  an increase in drift orbit shift is expected for a fixed RE distribution. This has the effect of moving the synchrotron patterns towards the low-field side, opposite to our observations. SOFT modelling was used to verify that the two effects above do indeed not explain the observed changes in synchrotron patterns. Lastly, the time-varying magnetic field can affect the distribution of RE momentum over the  $p_{\parallel}$  and  $p_{\perp}$  components through the conservation of the magnetic moment. However, a ramp-down in the magnetic field should yield a reduced  $p_{\perp}$ , which opposes the increasing pitch angle observed in the experiment presented here. Also, the inclusion of this mechanism in DREAM indicates that the effect on the distribution is negligible compared to the much faster collisional equilibration.

Another point for discussion is the role of the reconstructed radial profile. A decrease in vortex momentum could be indicative of a radial re-distribution of the REs towards the edge of the plasma, where  $p_{\parallel, nm}$  is smaller. However, the corresponding change in the synthetic synchrotron images does not resemble the experimental observations, and the reconstruction algorithm does indeed not show an appreciable change in radial profile.

The above considerations indicate that the match in vortex momentum between the experiment and model is robust evidence for toroidal field ripple-induced RE scattering. The inferred trend of increasing pitch angles during a magnetic field ramp-down supports this statement, while the mismatch in absolute value is attributable to simplifications made in the ripple model.

The conclusions drawn here could be reinforced through additional diagnostic coverage for the RE population. Time-resolved reconstructions of the RE bremsstrahlung can help estimate the maximum RE energy. This way, we can assess if the parallel momentum is indeed sufficient to reach the ripple resonance during experiments as the kinetic model and time-integrated loop voltage suggest. Furthermore, this information would help to assess if the pitch angle scattering indeed results in a hard energy limit.

The narrow energy distribution of the REs in the momentum-space vortex can yield amplification of their spontaneous microwave emission. While such radiation from the plasma core will likely be re-absorbed, contributions from the edge can escape the plasma [31]. Assuming a mono-energetic vortex, this RE ‘maser’ radiation would, for TCV, have a frequency in the range of a few GHz at the plasma edge. During the magnetic field ramp-down, we calculate a  $\sim 20\%$  decline in the microwave frequency, which could be detected in the presence of a suitable sensor.

In support of earlier work [31–33], observations and analysis reported herein suggest that accounting for ripple resonance may be important when interpreting RE synchrotron observations. As conveyed by equation (5), the resonant momentum increases in proportion to the machine parameter  $BR/N_c$ . This likely renders the ripple resonance irrelevant for commercial-scale tokamaks. In ITER, the  $n = 1$  resonance is found at  $p_{\parallel, nm}/m_e c \approx 1000$ , for which the RE drift orbit will have already intersected the wall. Only higher-order modes can be accessed, but the corresponding ripple strength and, thus, scattering efficiency will be limited. Nevertheless, other RE-driven [34–36] or deliberately induced [21, 37–40] high-frequency instabilities could be invoked to manipulate RE energies through pitch angle scattering induced synchrotron losses, in order to minimise damage to the plasma-facing wall and underlying components [41]. The present work provides direct experimental evidence of such RE momentum-space engineering.

## Acknowledgments

This work has been carried out within the framework of the EUROfusion Consortium, partially funded by the European Union via the Euratom Research and Training Programme (Grant Agreement No. 101052200 - EUROfusion). The Swiss contribution to this work has been funded by the Swiss State Secretariat for Education, Research and Innovation (SERI). Views and opinions expressed are however those of the author(s) only and do not necessarily reflect those of the European Union, the European Commission or SERI. Neither the European Union nor the European Commission nor SERI can be held responsible for them. This work was supported in part by the Swiss National Science Foundation.

## ORCID iDs

T.A. Wijkamp  <https://orcid.org/0000-0003-3110-8682>

M. Hoppe  <https://orcid.org/0000-0003-3994-8977>

J. Decker  <https://orcid.org/0000-0003-0220-2653>  
 B.P. Duval  <https://orcid.org/0000-0001-7783-129X>  
 A. Perek  <https://orcid.org/0000-0002-4117-0298>  
 U. Sheikh  <https://orcid.org/0000-0001-6207-2489>  
 I.G.J. Classen  <https://orcid.org/0000-0001-8982-8856>  
 R.J.E. Jaspers  <https://orcid.org/0000-0002-0589-7836>

## References

- [1] Hoppe M., Ekmark I., Berger E. and Fülöp T. 2022 Runaway electron generation during tokamak start-up *J. Plasma Phys.* **88** 905880317
- [2] Vallhagen O., Embreus O., Pusztai I., Hesslow L. and Fülöp T. 2020 Runaway dynamics in the DT phase of ITER operations in the presence of massive material injection *J. Plasma Phys.* **86** 475860401
- [3] Berger E., Pusztai I., Newton S.L., Hoppe M., Vallhagen O., Fil A. and Fülöp T. 2022 Runaway dynamics in reactor-scale spherical tokamak disruptions *J. Plasma Phys.* **88** 905880611
- [4] Perek A. *et al* 2019 MANTIS: a real-time quantitative multispectral imaging system for fusion plasmas *Rev. Sci. Instrum.* **90** 123514
- [5] Reimerdes H. *et al* 2022 Overview of the TCV tokamak experimental programme *Nucl. Fusion* **62** 042018
- [6] Hoppe M., Papp G., Wijkamp T., Perek A., Decker J., Duval B., Embreus O., Fülöp T. and Sheikh U.A. (The TCV team and The EUROfusion MST1 team) 2020 Runaway electron synchrotron radiation in a vertically translated plasma *Nucl. Fusion* **60** 094002
- [7] Wijkamp T.A., Perek A., Decker J., Duval B., Hoppe M., Papp G., Sheikh U.A., Classen I.G.J. and Jaspers R.J.E. (The TCV Team and The EUROfusion MST1 Team) 2021 Tomographic reconstruction of the runaway distribution function in TCV using multispectral synchrotron images *Nucl. Fusion* **61** 046044
- [8] Kurzan B., Steuer K.H. and Fussmann G. 1995 Dynamics of runaway electrons in the magnetic field of a tokamak *Phys. Rev. Lett.* **75** 4626–9
- [9] Hoppe M., Embreus O. and Fülöp T. 2021 DREAM: a fluid-kinetic framework for tokamak disruption runaway electron simulations *Comput. Phys. Commun.* **268** 108098
- [10] Rax J.M., Fisch N.J. and Laurent L. 1993 Fast particle resonances in tokamaks *Plasma Phys. Control. Fusion* **35** B129
- [11] Hesslow L., Unnerfelt L., Vallhagen O., Embreus O., Hoppe M., Papp G. and Fülöp T. 2019 Evaluation of the Dreicer runaway generation rate in the presence of high-Z impurities using a neural network *J. Plasma Phys.* **85** 475850601
- [12] Hesslow L., Embreus O., Vallhagen O. and Fülöp T. 2019 Influence of massive material injection on avalanche runaway generation during tokamak disruptions *Nucl. Fusion* **59** 084004
- [13] Pike O.J. and Rose S.J. 2014 Dynamical friction in a relativistic plasma *Phys. Rev. E* **89** 053107
- [14] Boozer A.H. 2005 Physics of magnetically confined plasmas *Rev. Mod. Phys.* **76** 1071–141
- [15] Laurent L. and Rax J.M. 1990 Stochastic instability of runaway electrons in tokamaks *Europhys. Lett.* **11** 219
- [16] Martín-Solís J.R., Esposito B., Sánchez R. and Alvarez J.D. 1999 Energy limits on runaway electrons in tokamak plasmas *Phys. Plasmas* **6** 238–52
- [17] Decker J. *et al* (The TCV Team and the EUROfusion MST1 Team) 2022 Full conversion from ohmic to runaway electron driven current via massive gas injection in the TCV tokamak *Nucl. Fusion* **62** 076038

- [18] Decker J., Hirvijoki E., Embreus O., Peysson Y., Stahl A., Pusztai I. and Fülöp T. 2016 Numerical characterization of bump formation in the runaway electron tail *Plasma Phys. Control. Fusion* **58** 025016
- [19] Guo Z., McDevitt C.J. and Tang X.-Z. 2017 Phase-space dynamics of runaway electrons in magnetic fields *Plasma Phys. Control. Fusion* **59** 044003
- [20] Guo Z., Tang X.-Z. and McDevitt C.J. 2017 Models of primary runaway electron distribution in the runaway vortex regime *Phys. Plasmas* **24** 112508
- [21] Guo Z., McDevitt C.J. and Tang X.-Z. 2018 Control of runaway electron energy using externally injected whistler waves *Phys. Plasmas* **25** 032504
- [22] Hoppe M., Embréus O., Paz-Soldan C., Moyer R.A. and Fülöp T. 2018 Interpretation of runaway electron synchrotron and bremsstrahlung images *Nucl. Fusion* **58** 082001
- [23] Hoppe M. et al 2021 Spatiotemporal analysis of the runaway distribution function from synchrotron images in an ASDEX Upgrade disruption *J. Plasma Phys.* **87** 855870102
- [24] Hoppe M., Embréus O., Tinguely R.A., Granetz R.S., Stahl A. and Fülöp T. 2018 SOFT: a synthetic synchrotron diagnostic for runaway electrons *Nucl. Fusion* **58** 026032
- [25] Andersen A.H. and Kak A.C. 1984 Simultaneous algebraic reconstruction technique (SART): a superior implementation of the ART algorithm *Ultrason. Imaging* **6** 81–94
- [26] Lu W. and Yin F.F. 2004 Adaptive algebraic reconstruction technique *Med. Phys.* **31** 3222–30
- [27] Karhunen J. et al 2019 Effect of reflections on 2D tomographic reconstructions of filtered cameras and on interpreting spectroscopic measurements in the JET ITER-like wall divertor *Rev. Sci. Instrum.* **90** 103504
- [28] Maretzke S. 2019 Generalized SART methods for tomographic imaging (arXiv:1803.04726)
- [29] Hirvijoki E., Asunta O., Koskela T., Kurki-Suonio T., Miettunen J., Sipilä S., Snicker A. and Äkäslompolo S. 2014 ASCOT: solving the kinetic equation of minority particle species in tokamak plasmas *Comput. Phys. Commun.* **185** 1310–21
- [30] Fülöp T., Pokol G., Helander P. and Lisak M. 2006 Destabilization of magnetosonic-whistler waves by a relativistic runaway beam *Phys. Plasmas* **13** 06
- [31] Kurzan B., Steuer K.-H. and Suttrop W. 1997 Runaway electrons in a tokamak: a free-electron maser *Rev. Sci. Instrum.* **68** 423–6
- [32] Jaspers R.J.E. 1995 Relativistic runaway electrons in tokamak plasmas *PhD Thesis* Eindhoven University of Technology, Department of Applied Physics
- [33] Chen Z.Y., Wan B.N., Shi Y.J., Ju H.J., Zhu J.X. and Liang H.F. 2009 Resonant interaction of runaway electrons with magnetic field ripple in tokamak plasmas *J. Plasma Phys.* **75** 669–74
- [34] Buratti P. et al 2021 Fast dynamics of radiofrequency emission in FTU plasmas with runaway electrons *Plasma Phys. Control. Fusion* **63** 095007
- [35] Bin W., Castaldo C., Napoli F., Buratti P., Cardinali A., Selce A. and Tudisco O. 2022 First intrashot observation of runaway-electron-driven instabilities at the lower-hybrid frequency range under ITER-relevant plasma-wave dispersion conditions *Phys. Rev. Lett.* **129** 045002
- [36] Lvovskiy A. et al 2023 Parametric study of Alfvénic instabilities driven by runaway electrons during the current quench in DIII-D *Nucl. Fusion* **63** 046011
- [37] Liu C., Hirvijoki E., Fu G.-Y., Brennan D.P., Bhattacharjee A. and Paz-Soldan C. 2018 Role of kinetic instability in runaway-electron avalanches and elevated critical electric fields *Phys. Rev. Lett.* **120** 265001
- [38] Dae Yoon Y., Ji J.-Y. and Yun G.S. 2021 Deterministic scattering of relativistic electron beams by off-resonant circularly polarized electromagnetic waves *Phys. Plasmas* **28** 060702
- [39] Heidbrink W.W., Paz-Soldan C., Spong D.A., Du X.D., Thome K.E., Austin M.E., Lvovskiy A., Moyer R.A., Pinsker R.I. and Van Zeeland M.A. 2018 Low-frequency whistler waves in quiescent runaway electron plasmas *Plasma Phys. Control. Fusion* **61** 014007
- [40] Liu C., Brennan D.P., Lvovskiy A., Paz-Soldan C., Fredrickson E.D. and Bhattacharjee A. 2021 Compressional Alfvén eigenmodes excited by runaway electrons *Nucl. Fusion* **61** 036011
- [41] Sizyuk V. and Hassanein A. 2009 Self-consistent analysis of the effect of runaway electrons on plasma facing components in ITER *Nucl. Fusion* **49** 095003